PHYSICAL REVIEW E **105**, 065201 (2022)

# Nonlinear Thomson scattering with ponderomotive control

D. Ramsey,[1,*] B. Malaca,[2] A. Di Piazza,[3] M. Formanek,[3] P. Franke,[1] D. H. Froula,[1] M. Pardal,[2] T. T. Simpson,[1] J. Vieira,[2]
K. Weichman,[1] and J. P. Palastro[1,†]
[1] *Laboratory for Laser Energetics, University of Rochester, Rochester, New York 14623, USA*
[2] *GoLP/Instituto de Plasmas e Fusão Nuclear, Instituto Superior Técnico, Universidade de Lisboa, Lisbon 1049-001, Portugal*
[3] *Max-Planck-Institut für Kernphysik, Saupfercheckweg 1, D-69117 Heidelberg, Germany*

(Received 28 September 2021; revised 23 February 2022; accepted 2 May 2022; published 6 June 2022;
corrected 2 September 2022 and 6 January 2023)

In nonlinear Thomson scattering, a relativistic electron reradiates the photons of a laser pulse, converting optical light to x rays or beyond. While this extreme frequency conversion offers a promising source for probing high-energy-density materials and driving uncharted regimes of nonlinear quantum electrodynamics, conventional nonlinear Thomson scattering has inherent trade-offs in its scaling with laser intensity. Here we discover that the ponderomotive control afforded by spatiotemporal pulse shaping enables regimes of nonlinear Thomson scattering that substantially enhance the scaling of the radiated power, emission angle, and frequency with laser intensity. By appropriately setting the velocity of the intensity peak, a spatiotemporally shaped pulse can increase the power radiated by orders of magnitude. The enhanced scaling with laser intensity allows for operation at significantly lower electron energies or intensities.

DOI: 10.1103/PhysRevE.105.065201

Bright sources of high-energy photons lead to advancements in a range of disciplines, including ultrafast biology and material science, nonlinear quantum electrodynamics, nuclear spectroscopy, and radiotherapy [1–13]. The brightest sources currently reside at large accelerator facilities in the form of x-ray free-electron lasers or synchrotrons [14–16]. Laser-driven sources [17–39] promise a smaller-scale, widely accessible alternative but face challenges in achieving the required photon number, energy, and coherence. Of the potential candidates, nonlinear Thomson scattering (NLTS) can produce extremely high energy, collimated radiation in a relatively controlled setting [18–20,25,27,30,33,36,37,39]. Like the other candidates, however, NLTS has inherent constraints that can impede its realization as a practical light source.

In NLTS, a relativistic electron collides with a laser pulse traveling in the opposite direction [Fig. 1(a)]. The electron rapidly oscillates in the fields of the pulse and reradiates the incident photons. The properties of the radiation depend on the vector potential $a$ and frequency $\omega_0$ of the pulse and the initial electron energy $\gamma_0$ (energy and charge are normalized to $m_e c^2$ and $e$ throughout). Maximizing the radiated power $P$, or the number of photons, requires large vector potentials ($P \propto a^2$). In these strong fields ($a \gg 1$), the ponderomotive force of the pulse appreciably decelerates the electron and increases the amplitude of its oscillations along the direction of its initial motion [17,19]. This redshifts the emitted frequencies $\omega_n$ and widens the emission angle $\theta_e$: $\omega_n \approx 8n\gamma_0^2\omega_0/a^2$ and $\theta_e \sim a/\gamma_0$, where $n$ is an integer [19]. This trade-off between the power, spectrum [40], and emission angle constrains the utility of NLTS.

Spatiotemporal pulse shaping provides control over the ponderomotive force, which can compensate the ponderomotive deceleration in NLTS [41–48]. As an example, the chromatic aberration of a diffractive optic and a chirp can be used to control the location and time at which each temporal slice within a pulse comes to its focus, respectively [42,43]. By adjusting the chirp, the resulting intensity peak, and therefore the ponderomotive force, can travel at any velocity, either forward or backward with respect to the phase fronts, over distances much longer than a Rayleigh range [42,43]. Aside from extending the interaction length, a ponderomotive force that counterpropagates with respect to the phase fronts can *accelerate* an electron in NLTS [49] and can provide unique insight into the corresponding quantum process, i.e., nonlinear Compton scattering [50].

Here we describe regimes of nonlinear Thomson scattering that exploit the ponderomotive control afforded by spatiotemporal pulse shaping to substantially enhance the scaling of power, emission angle, and frequency with laser intensity. For high-intensity pulses ($a^2 \gg 1$), these regimes exhibit orders of magnitude higher radiated powers, better efficiency, and smaller emission angles than conventional NLTS at the cost of more laser pulse energy. When compared at the same laser energy, the improved scalings allow for the use of lower electron energies or intensities. While the results are generalized to any ponderomotive velocity $\beta_I = v_I/c$, we focus on two regimes: "drift-free" NLTS, which preserves spectral properties independent of the laser pulse shape and intensity, and "matched" NLTS, which offers a spectrum that can be tuned independently of the initial electron energy. This approach to NLTS compliments existing techniques that employ tailored frequency chirps to mitigate line broadening and compensate

---

[*] dram@lle.rochester.edu
[†] jpal@lle.rochester.edu

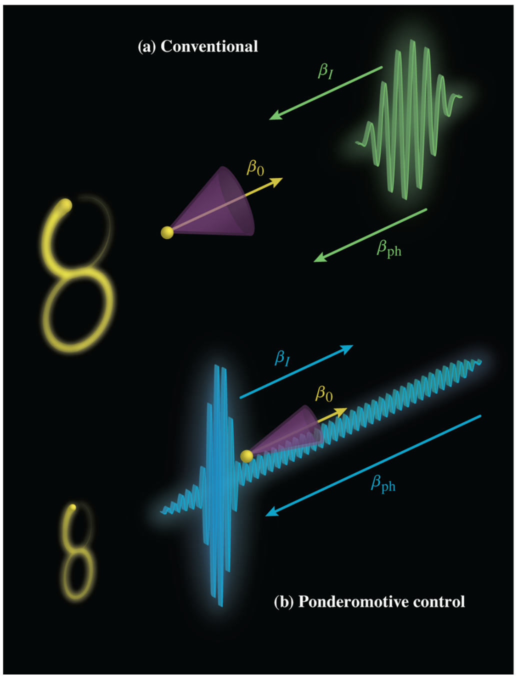

FIG. 1. (a) A conventional NLTS configuration in which the intensity peak and phase fronts of a laser pulse travel in the opposite direction as the electron. At the rising edge of the intensity peak, the ponderomotive force decelerates the electron, redshifting the emitted frequencies and widening their emission angle (purple cone). (b) NLTS with ponderomotive control aligns the velocities of the intensity peak and the electron. Here the ponderomotive force increases or maintains the electron velocity, allowing for higher-frequency emission into a smaller angle. The electron trajectory in its average rest frame (figure eight) is depicted to the left of each case.

redshifting in the mildly nonlinear regime of Thomson scattering ($a \lesssim 1$) [51–54].

Figure 1 contrasts backscattering configurations for conventional NLTS and NLTS with ponderomotive control (NPC). Conventional NLTS employs a standard laser pulse with an intensity peak and phase that counterpropagate at the vacuum speed of light with respect to a relativistic electron. NPC employs a spatiotemporally shaped pulse with an intensity peak that counterpropagates with respect to its phase fronts and copropagates with respect to the electron. In both cases, as the electron enters the leading edge of the intensity peak, it begins oscillating in the polarization (transverse) and propagation (longitudinal) directions. For a linearly polarized pulse, the motion in a frame moving with the average longitudinal velocity of the electron traces out a figure eight. NPC provides additional freedom over this motion.

The electron trajectory evolves in response to the vector potential $\mathbf{a} = a(z - \beta_I t)\cos(z + t)\hat{x}$, where the envelope $a$ captures the motion of the intensity peak and time and space have been normalized to $\omega_0$ and $\omega_0/c$, respectively (Appendix A). Recognizing that the vector potential changes slowly with the coordinate $\xi = z - \beta_I t$ and rapidly with $\eta = z + t$, a multiple-timescale analysis reveals the local conservation equation $\gamma + u_z \equiv h(\xi)$, where $\mathbf{u}$ is the electron momentum. This relation indicates that the Hamiltonian $h$ of the electron in a frame moving with the phase velocity depends only on the slow coordinate $\xi$. Using this relation, one can show that

$$h(\xi) = \langle\gamma\rangle(1 + \beta_I^{-1}) + \gamma_0(\beta_0 - \beta_I^{-1}), \tag{1}$$

where $\langle\gamma\rangle = \gamma_I^2\gamma_0(1 - \beta_I\beta_0) - \beta_I\gamma_I^2[\gamma_0^2(1 - \beta_I\beta_0)^2 - \gamma_I^{-2}\langle\gamma_\perp^2\rangle]^{1/2}$ is the electron energy averaged over a cycle of the laser pulse, $\beta_0 = (1 - \gamma_0^{-2})^{1/2}$ is the initial longitudinal velocity of the electron, $\gamma_I^2 = (1 - \beta_I^2)^{-1}$, and $\langle\gamma_\perp^2\rangle = 1 + \frac{1}{2}a^2$. Note that $h$ depends only on the initial electron energy, the ponderomotive velocity, and the local value of the vector potential. From here on, the $\xi$ dependence of all quantities that depend on $a$ is understood.

The Hamiltonian $h$ determines all details of the electron trajectory and the radiation properties. Specifically, the radiation results from the time-dependent curvature of the electron trajectory, which is set by the amplitudes of the transverse ($x_0$) and longitudinal ($z_0$) oscillations, $x_0 = a/h$ and $z_0 = a^2/8h^2$, about a drift motion characterized by the longitudinal velocity, $\beta_d = (h^2 - \langle\gamma_\perp^2\rangle)/(h^2 + \langle\gamma_\perp^2\rangle)$ [19]. The cycle-averaged power, emission angle, harmonic frequency, and bandwidth $\omega_b$ all depend on $h$: $\langle P\rangle = r_e h^2 a^2/3$, $\theta_e \backsim a/h$, $\omega_n = nh^2/\langle\gamma_\perp^2\rangle$, and $\omega_b = 3a^3h^2/4\langle\gamma_\perp^2\rangle$, where $r_e$ is the classical electron radius. Conventional NLTS corresponds to the special case of $\beta_I = -1$ and $h = (1 + \beta_0)\gamma_0$ with the radiation properties found in Table I. Through $h$, the ponderomotive velocity $\beta_I$ provides an additional parameter to tune the trajectory and radiation properties.

Figure 2 illustrates the impact of using the ponderomotive velocity to tune the electron trajectory. For ponderomotive velocities parallel to the initial electron velocity, the radiated power can be orders of magnitude larger than in conventional NLTS $\langle P_C\rangle$. Further, the enhancement in the radiated power increases with the vector potential $a$, favoring high-intensity laser pulses. Note that here and throughout, the parameters have been chosen to ensure that NLTS occurs in the classical regime, i.e., $\hbar\omega_b \ll \gamma_0$ [55].

To understand how the ponderomotive velocity changes the radiation properties, consider the longitudinal drift velocity of the electron $\beta_d$. The velocity can increase or decrease as the electron enters the intensity peak, depending on the value of $\beta_I$. In conventional NLTS, $h$ is independent of $a$. As a result, the increase in $\langle\gamma_\perp^2\rangle$ as the electron enters the pulse necessarily decreases $\beta_d$. Said differently, the electron is ponderomotively decelerated by the countertraveling intensity peak. In NPC, $\beta_I \approx 1$, and $h(\xi)$ depends on $a$. Now $h(\xi)$ and, as a result, $\beta_d$ increase as the electron enters the intensity peak; that is, the electron is ponderomotively accelerated by the cotraveling intensity peak. In fact, this acceleration can become so large that the electron outruns the intensity peak (gray area in Fig. 2). An increase in $\beta_d$, and therefore $h$, enhances the scaling of the radiation properties ($\langle P\rangle$, $\omega_n$, $\omega_b \propto h^2$ and $\theta_e \propto h^{-1}$). Two specific cases illustrate this benefit more clearly.

Drift-free NLTS employs a superluminal intensity peak to compensate the ponderomotive deceleration of the electron. When $\beta_I = \beta_0^{-1}$, the ponderomotive force increases the energy and the longitudinal momentum of the electron in the right balance to maintain a constant $\beta_d$ throughout the interaction (Fig. 2, inset). The resulting value of $h = (1 + \beta_0)\gamma_0\langle\gamma_\perp^2\rangle^{1/2}$ provides the radiation properties displayed in

TABLE I. Cycle-averaged power $\langle P\rangle$, emission angle $\theta_e$, harmonic frequency $\omega_n$, and bandwidth $\omega_b$ for conventional, drift-free, and matched NLTS. Here $\theta_e$ indicates the angle in the plane of the laser polarization and electron motion ($x$-$z$); the angle in the plane perpendicular to this ($y$-$z$) is smaller by $\approx 1/a$. For matched NLTS, it has been assumed that the electron spends most of the interaction at $a \approx a_0$.

| | Conventional | Drift free | Matched |
|---|---|---|---|
| $\langle P\rangle$ | $\frac{r_e}{3}(1+\beta_0)^2\gamma_0^2 a^2$ | $\frac{r_e}{3}(1+\beta_0)^2\gamma_0^2\left(1+\frac{1}{2}a^2\right)a^2$ | $\frac{r_e}{3}(1+\beta_I)^2\gamma_I^2\left(1+\frac{1}{2}a_0^2\right)a_0^2$ |
| $\theta_e$ | $\frac{a}{(1+\beta_0)\gamma_0}$ | $\frac{a}{(1+\beta_0)\gamma_0\left(1+\frac{1}{2}a^2\right)^{1/2}}$ | $\frac{a_0}{(1+\beta_I)\gamma_I\left(1+\frac{1}{2}a_0^2\right)^{1/2}}$ |
| $\omega_n$ | $\frac{n(1+\beta_0)^2\gamma_0^2}{1+\frac{1}{2}a^2}$ | $n(1+\beta_0)^2\gamma_0^2$ | $n(1+\beta_I)^2\gamma_I^2$ |
| $\omega_b$ | $\frac{3(1+\beta_0)^2\gamma_0^2 a^3}{4\left(1+\frac{1}{2}a^2\right)}$ | $\frac{3}{4}(1+\beta_0)^2\gamma_0^2 a^3$ | $\frac{3}{4}(1+\beta_I)^2\gamma_I^2 a_0^3$ |

Table I. Each property has an improved scaling with laser intensity $a^2$ when compared to conventional NLTS. Aside from the enhanced power (Fig. 2), the radiation in drift-free NLTS is emitted into a much smaller angle when $a \gg 1$ (see Fig. 3). Further, regardless of the time-dependent vector potential experienced by the electron, the harmonic frequencies remain fixed (Table I).

Matched NLTS uses a subluminal intensity peak to ponderomotively accelerate the electron. Here the intensity peak intercepts the electron from behind and gradually accelerates it to an asymptotic velocity $\beta_d = \beta_I$. This allows the electron to experience a near-constant vector potential for an extended distance (Fig. 2, inset). Setting the ponderomotive velocity to satisfy $(\beta_I - \beta_0)\gamma_I\gamma_0 = a_0/\sqrt{2}$ ensures that the electron cotravels with the intensity peak near the maximum vector potential $a_0$. With this condition met, $h = (1+\beta_I)\gamma_I\langle\gamma_\perp^2\rangle^{1/2}$, yielding the radiation properties found in Table I.

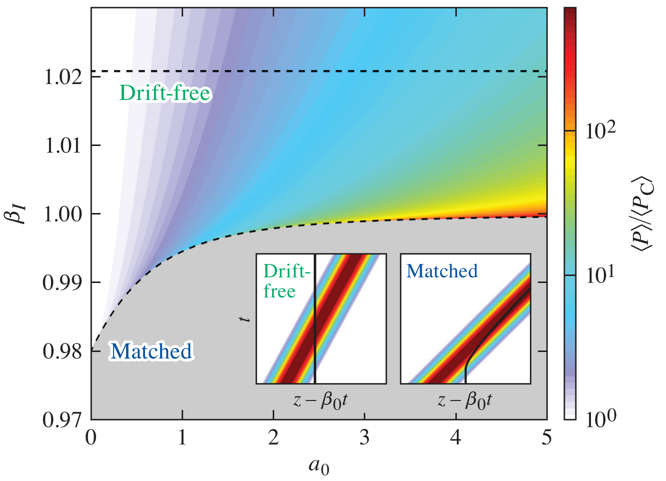

FIG. 2. Cycle-averaged radiated power as a function of the ponderomotive velocity $\beta_I$ and the vector potential $a$ normalized to power radiated in conventional NLTS $\langle P_C\rangle$. Here $\gamma_0 = 5$, and for the purpose of calculating $\langle P_C\rangle$, $\beta_I = -1$. The dashed lines indicate the matched and drift-free conditions. Within the gray region, the ponderomotive force accelerates the electron to a velocity greater than $\beta_I$, and the electron outruns the intensity peak [49]. The insets depict the cycle-averaged electron trajectories (black lines) relative to the motion of the intensity peak (contours).

Matched NLTS represents the optimal case of NPC. With a smaller ponderomotive velocity, the electron would outrun the intensity peak; with a larger, but still subluminal, ponderomotive velocity, the intensity peak would overtake and outrun the electron, limiting the interaction length [49,56]. For large vector potentials ($a_0 \gg 1$), the optimal scalings (Table I) result in a radiated power far greater and an emission cone far narrower than either drift-free or conventional NLTS (Figs. 2 and 3). In this limit, $\gamma_I \simeq \sqrt{2}a_0\gamma_0$, such that $\langle P\rangle \propto a_0^6$, $\theta_e \propto a_0^{-1}$, $\omega_n \propto a_0^2$, and $\omega_b \propto a_0^5$.

Copropagation of the electron and intensity peak in NPC extends the maximum interaction length $L$ and duration of the radiation [$t_r \sim (1-\beta_d)L$] beyond that of conventional NLTS, which increases the total radiated energy ($U_r \sim LP$). For an intensity peak of duration $\tau$ (FWHM), $L_C \sim \tau/2$ and $L_D \sim \gamma_0^2\tau$ in conventional and drift-free NLTS, respectively. Matched NLTS requires an initial distance $L_M \sim a_0^2\gamma_0^2\tau$ for the intensity peak to accelerate the electron to its asymptotic velocity. In principle, once this velocity is reached, the interaction length is unbounded.

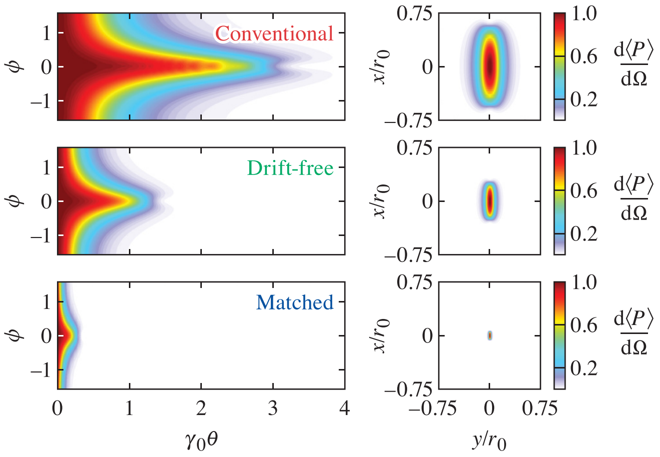

FIG. 3. Left: Power radiated per steradian as a function of the angle with respect to the initial electron velocity $\theta$ and the angle coplanar with the laser polarization $\phi$ for $\gamma_0 = 5$ and $a_0 = 3$. Right: The projection of the radiated power on a plane located a distance $r_0$ from the source. Each plot has been normalized to its maximum value: 0.016, 0.50, 204 MeV sr$^{-1}$ ps$^{-1}$ for conventional, drift-free, and matched NLTS, respectively.

Despite the enhanced scalings in NPC, the rate of photon emission $\dot{N}$ is identical to that in conventional NLTS. For $a \gg 1$, $\dot{N} \sim \langle P\rangle/\hbar\omega_b = 2r_e a/9$ (or, more exactly, $3.5 \times 10^{14}$ photons/s per electron for each case in Fig. 3). This indicates that the enhanced power in NPC results from the emitted photons having higher frequencies—not the emission of more photons. Even with the same rate of photon emission, NPC can produce more total photons because of the longer interaction lengths ($N \sim La$). For conventional, drift-free, and matched NLTS, $N_C \sim \tau a_0$, $N_D \sim \tau\gamma_0^2 a_0$, and $N_M \sim \tau\gamma_0^2 a_0^3$.

The extended interaction lengths in NPC do, however, come with a caveat: for the same intensity, a spatiotemporally shaped pulse must have more energy than a conventional pulse to sustain its intensity over the interaction distance. This is because the energy is spread longitudinally over the interaction distance [42,43]. Specifically, the pulse energies for conventional and shaped pulses are given by $U_{pC} = \tau w_0^2 a_0^2/16r_e$ and $U_{pS} = L w_0^2 a_0^2/4r_e$, where $w_0$ is the focal spot size and the shaped pulse includes the energy required for transverse shaping (Appendix B). Setting the duration of the conventional pulse equal to twice the Rayleigh range to maximize efficiency and noting that the intensity peak duration of the shaped pulse is given by $\tau = 2w_0^2$ [48,57] provide the required energies: $U_{pC} = \tau^2 a_0^2/16r_e$, $U_{pD} = \tau^2\gamma_0^2 a_0^2/8r_e$, and $U_{pM} > \tau^2\gamma_0^2 a_0^4/8r_e$. At fixed intensity and electron energy, $U_{pD}/U_{pC} = 2\gamma_0^2$, and $U_{pM}/U_{pC} > 2\gamma_0^2 a_0^2$. Despite the larger energy requirement, the shaped pulses can have higher efficiencies ($\epsilon = U_r/U_p$): $\epsilon_C = 32r_e^2\gamma_0^2/3\tau$, $\epsilon_D = 16r_e^2\gamma_0^2 a_0^2/3\tau$, and $\epsilon_M = 32r_e^2\gamma_0^2 a_0^4/3\tau$.

Instead of operating at the same laser intensity and electron energy, one can compare conventional NLTS and NPC for fixed laser energy and electron energy. Setting $U_{pC} = U_{pS}$ provides $a_{0D} = \sqrt{2}\gamma_0(L_C/L_D)a_{0C}$ and $1 = \sqrt{2}\gamma_0(L_C/L_M)a_{0C}$ for drift-free and matched NLTS, respectively. For a desired bandwidth with $a_0^2 \gg 1$, $a_{0D}^3 = 2a_{0C}$, and $a_{0M}^5 = a_{0C}$, providing $U_{rD}/U_{rC} = \sqrt{2}\gamma_0$ and $U_{rM}/U_{rC} = \sqrt{2}\gamma_0 a_{0C}^{1/5}$. At fixed laser pulse energy, NPC produces more radiated energy than conventional NLTS.

The advantage of NPC occurs for high-energy laser pulses. As an example, consider a $\lambda_0 = 1.054\,\mu$m wavelength pulse with $U_p = 580$ J and a 2.5 MeV ($\gamma_0 = 5$) electron. A spatiotemporally shaped pulse designed for drift-free NLTS (Appendix B) with $a_{0D} = 3$ and $L_D = 8$ mm ($\tau = 1$ ps and $P = 9$ TW) has the same energy as a conventional pulse with $a_{0C} = 13.5$ and $L_C = 250\,\mu$m ($\tau = 1.7$ ps). In this case, drift-free NLTS radiates ~7 times more energy than conventional NLTS into an ~10 times smaller emission angle.

A similar comparison can be made for matched NLTS at a larger pulse energy. For a $U_p = 4.5$ kJ pulse and a 2.5 MeV electron, a pulse designed for matched NLTS with $a_{0M} = 3$ and $L_M = 7$ cm ($\tau = 1$ ps and $P = 9.5$ TW) has the same energy as a conventional pulse with $a_{0C} = 240$ and $L_C = 40\,\mu$m ($\tau = 270$ fs). In this case, matched NLTS radiates ~20 times more energy than conventional NLTS.

The plane wave model presented above accurately describes the electron motion and radiation properties when the transverse excursion of the electron is much smaller than the laser spot [see Appendix C for three-dimensional (3D) considerations]. To further verify this model and explore the effects of finite energy spread on NPC, OSIRIS simulations [58] were conducted using the RADIO package [38] (Appendix D). In both conventional NLTS and NPC, a single electron radiates a coherent spectrum with well-defined peaks (Fig. 4). While an energy spread of $\Delta\gamma/\gamma_0 = 1\%$ had little effect on the spectrum, $\Delta\gamma/\gamma_0 = 5\%$ was sufficient to blur each spectral peak (Fig. 4). For conventional NLTS, the proximity of the harmonics combined with the blurring ($\Delta\omega_n \sim 2\omega_n\Delta\gamma/\gamma_0$) created a near-continuous spectrum. For drift-free NLTS, the larger separation between the harmonics mitigated this effect. Matched NLTS also produces harmonics with a larger separation. However, electrons with different momenta experience different vector potentials along their trajectories, which contributes additional blurring.

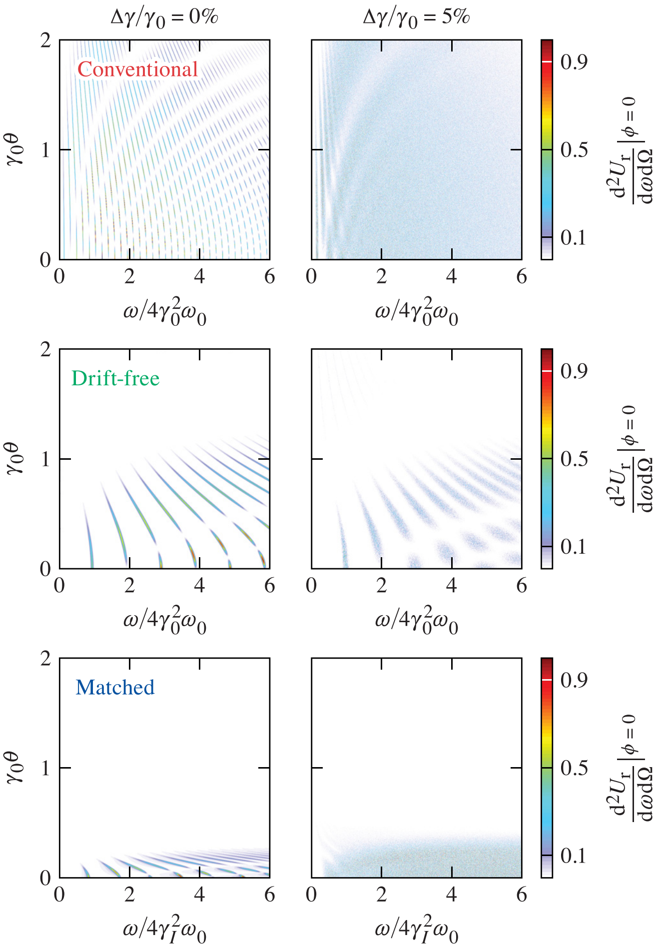

FIG. 4. Spectrum of emitted radiation from a collection of electrons with $\gamma_0 = 5$ and $a_0 = 3$. Left: No energy spread; right: $\Delta\gamma/\gamma_0 = 5\%$ all in the longitudinal momentum. The quantity $U_r$ has units of energy, and each plot is normalized to its maximum value. For matched NLTS, the horizontal axis is scaled to $4\gamma_l^2\omega_0$, not $4\gamma_0^2\omega_0$, and therefore extends to much higher frequencies.

The divergence of the electron bunch can also modify the radiation properties. In particular the bunch divergence will dominant the angular emission properties when the divergence angle, $\theta_D = \mathrm{atan}(u_\perp/u_z)$, exceeds the single electron emission angle $\theta_e$. While a large bunch divergence would eliminate the advantage of the smaller emission angle in NPC, the examples above would still result in greater total energies and brilliances than conventional NLTS.

NLTS has the potential to provide an alternative to light sources based on conventional accelerators with far-reaching benefits in medicine and basic science. NPC can produce high-energy photons with a spectrum that can be tuned through the initial electron energy, the laser amplitude, and, now, the ponderomotive velocity. This added flexibility mitigates trade-offs inherent in conventional NLTS. Specifically, the intensity peak of a laser pulse in conventional NLTS counterpropagates with respect to the electron, causing a ponderomotive deceleration that redshifts the radiation and widens the emission angle—an effect exacerbated by large laser intensities. By reversing the propagation direction of the intensity peak with respect to the phase fronts, a spatiotemporally shaped pulse can ponderomotively accelerate the electron. For drift-free NLTS, this removes the intensity dependence of the harmonic frequencies and emission angle while enhancing the intensity scaling of the bandwidth and power. For matched NLTS, this enhances the intensity scaling of all radiation properties.

The authors would like to thank M. Vranic, W. B. Mori, and J. Pierce for insightful and exciting discussions. This report was prepared as an account of work sponsored by an agency of the U.S. Government. Neither the U.S. Government nor any agency thereof, nor any of their employees, makes any warranty, express or implied, or assumes any legal liability or responsibility for the accuracy, completeness, or usefulness of any information, apparatus, product, or process disclosed, or represents that its use would not infringe privately owned rights. The views and opinions of authors expressed herein do not necessarily state or reflect those of the U.S. Government or any agency thereof. This material is based upon work supported by the Office of Fusion Energy Sciences under Awards No. DE-SC0019135 and No. DE-SC00215057, the Department of Energy National Nuclear Security Administration under Award No. DE-NA0003856, the University of Rochester, and the New York State Energy Research and Development Authority.

## APPENDIX A: FLYING FOCUS FOUR-POTENTIAL

A number of experiments have used spatiotemporal pulse shaping to create laser pulses with an intensity peak that moves with a controllable velocity, either forward or backward, over distances much greater than a Rayleigh range [41–43]. Over the region in which the intensity peak persists, each of these realizations can be modeled as a propagation invariant pulse. In vacuum, the four-potential in the Lorenz gauge [$A^\mu = (\Phi, \mathbf{A})$] satisfies the wave equation

$$(\nabla^2 - c^{-2}\partial_t^2)A^\mu(\mathbf{x}, t) = 0. \tag{A1}$$

Upon transforming to the coordinates $\eta = z + ct$ and $\xi = z - v_I t$, Eq. (A1) becomes

$$[\nabla_\perp^2 + (1-\beta_I^2)\partial_\xi^2 + 2(1+\beta_I)\partial_\eta\partial_\xi]A^\mu(\mathbf{x}_\perp, \eta, \xi) = 0, \tag{A2}$$

where $\beta_I = v_I/c$. When $\beta_I \approx 1$, which is the situation considered here, or in the paraxial limit, the $\partial_\xi^2$ term can be neglected. Expressing the four-potential as a rapidly varying carrier wave modulating an envelope, i.e., $A^\mu = \frac{1}{2}A^\mu(\mathbf{x}_\perp, \xi)e^{-ik_0\eta} + \text{c.c.}$, with $k_0 = \omega_0/c$, and substituting into Eq. (A2) provide

$$[\nabla_\perp^2 - 2i\omega_0(1+\beta_I)\partial_\xi]A^\mu(\mathbf{x}_\perp, \xi) = 0. \tag{A3}$$

Solutions to Eq. (A3) can be written as superpositions of Laguerre-Gaussian modes. For a laser pulse composed of a single mode and polarized in the $x$ direction, the envelope of the transverse potential has the explicit form

$$\begin{aligned} A_x(r,\theta,\xi) = A_0 \frac{w_0}{w(\xi)}\left[\frac{\sqrt{2}r}{w(\xi)}\right]^\ell L_n^\ell\left[\frac{2r^2}{w^2(\xi)}\right] \\ \times \exp\left[-\left(1+i\frac{\xi}{\xi_0}\right)\frac{r^2}{w^2(\xi)}\right. \\ \left. - i\ell\theta + i(2n+\ell+1)\arctan\frac{\xi}{\xi_0}\right], \end{aligned} \tag{A4}$$

where $L_n^\ell$ is a Laguerre polynomial, $n$ is the radial quantum number, $\ell$ is the orbital angular momentum quantum number, $w(\xi) = w_0\sqrt{1+\xi^2/\xi_0^2}$, $w_0$ is the spot size at focus, and $\xi_0 = k_0(1+\beta_I)w_0^2/2$ (note $\xi_0 = \tau/2$, where $\tau$ is the FWHM duration of the intensity peak). With the transverse vector potential specified, $A_z$ and $\Phi$ are exactly determined through the Lorenz gauge conditions $\Phi = A_z/\beta_I$ and $ik_0(1+\beta_I^{-1})A_z = -\partial_x A_x$. These exact expressions for $A_x$, $\Phi$, and $A_z$ facilitate calculations of the electron trajectories.

The solution limits to $A_x = A(z - v_I t)\cos[k_0(z+ct)]$ as $r \to 0$ and for $\xi \approx 0$, i.e., near the peak of the transverse potential. Here the axial potential $A_z$ vanishes, and $\arctan(\xi/\xi_0) \approx 0$. Simulations that evolved electron trajectories in the full, 3D four-potentials were conducted to test the validity of using the simplified form of the vector potential, i.e., $A_x = A(z - v_I t)\cos[k_0(z+ct)]$. For electrons initialized close to the optical axis (defined as $r = 0$), there was no significant difference in the trajectories or radiation properties. The dynamics were dominated by the leading order terms in the transverse electric and magnetic fields, which result from $A_x$ alone.

When using only the lowest-order Gaussian mode ($n = \ell = 0$), the transverse ponderomotive force ($F_p \propto -\gamma^{-1}\nabla_\perp|\mathbf{A}|^2$) can expel low-energy electrons from the laser pulse before they undergo significant axial acceleration and have a chance to radiate. This expulsion can be completely eliminated by using orthogonally polarized Laguerre-Gaussian modes to create a transverse ponderomotive potential well. For instance, with appropriate amplitude weighting, an $n = \ell = 0$ mode polarized in the $x$ direction and an $n = 0$, $\ell = 1$ mode polarized in the $y$ direction can produce a ponderomotive potential well that confines electrons to the optical axis [59,60]. Simulations of electron trajectories in the full, 3D potentials prescribed in an manner analogous to that above indicate that the transverse oscillations in this well do not significantly alter the described dynamics or relevant radiation properties. The use of an orthogonally polarized mode does, however, increase the total laser energy needed for NPC by a factor of ≈2.

## APPENDIX B: PRACTICAL FLYING FOCUS EXAMPLE

Appendix A described a theoretical model for the vector potential of a flying focus pulse. This Appendix provides a practical example. In the near field (i.e., the optics plane), a flying focus pulse is created by applying a time-dependent focal length. Said differently, the optical assembly imparts a different wave front curvature to each temporal slice within the pulse. The time at which each temporal slice reaches its focus $t_f$ consists of two contributions: its time within the pulse $\eta/c$ and its focal length $f$ divided by the group velocity $v_g$. Differentiating the resulting expression, $t_f = (f/v_g) + (\eta/c)$, with respect to $f$ and rearranging terms provide $\frac{df}{d\eta} \equiv u = v_g v_I/c(v_g - v_I)$, where $v_I$ is the desired velocity of the focal point. Upon integrating with respect to $\eta$, one finds the required time-dependent focal length $f(\eta) = f_0 + u\eta$, where $f_0$ is the nominal focal length. The moving focal point creates an intensity peak that travels a distance $L$ determined by the pulse duration: $L = |u|(\eta_{\max} - \eta_{\min})$. The duration of this intensity peak $\tau$ corresponds to the time that it takes adjacent temporal slices within the pulse to come in and out of focus, i.e., $\tau = 2Z_R/c|u| = k_0 w_0^2/c|u|$, where $Z_R$ is the Rayleigh range, $w_0 = 4k_0^{-1}F_N$, and $F_N$ is the $f$ number of the nominal lens.

The laser pulse starts in the near field ($z > f_0$) and propagates from right to left, i.e., in the negative $z$ direction, to the far field ($z \approx 0$). The transverse electric field of the pulse at the entrance to the optical assembly can be expressed as a rapidly oscillating carrier modulating an envelope: $\mathbf{E} = \frac{1}{2}e^{-ik_0\eta}\boldsymbol{E}(\mathbf{x}_\perp, \eta) + \text{c.c.}$ For nonlinear Thomson scattering with ponderomotive control, the intensity peak of a flying focus pulse must travel across the interaction length $L$ with a near-constant maximum intensity ($\propto a_0^2$) and with a flat or bowl-shaped transverse profile. A near-constant maximum intensity requires an initial laser pulse with a flat-top temporal profile. Here a super-Gaussian of order 8 is used: $\Theta(\eta) = \exp[-(2\eta/cT)^8]$. As discussed in Appendix A, a flat or bowl-shaped transverse profile can be achieved by using orthogonally polarized Laguerre-Gaussian modes with $n = \ell = 0$ and $n = 0$, $\ell = 1$. Combining these conditions provides the components of the envelope at the entrance to the optical assembly:

$$E_x = E_l \Theta(\eta) \exp\left(-\frac{r^2}{w_l^2}\right), \tag{B1}$$

$$E_y = \alpha E_l \Theta(\eta) \frac{\sqrt{2}r}{w_l} \exp\left(-\frac{r^2}{w_l^2} - i\theta\right), \tag{B2}$$

where $w_l$ and $E_l$ are the initial spot size and amplitude, respectively, and $\alpha \gtrsim 1$ is used to adjust the transverse shape of the ponderomotive force.

The optical assembly applies the time-dependent focal length. The frequency-domain envelope at the exit of the optical assembly (i.e., at $z = f_0$) is given by

$$\tilde{E}_x = E_l \tilde{\Theta}(\Omega) \exp\left[-\left(\frac{1}{w_l^2} + \frac{i\omega}{2cf_0}\right) r^2\right], \tag{B3}$$

$$\tilde{E}_y = \alpha E_l \tilde{\Theta}(\Omega) \frac{\sqrt{2}r}{w_l} \exp\left[-\left(\frac{1}{w_l^2} + \frac{i\omega}{2cf_0}\right) r^2 - i\theta\right], \tag{B4}$$

where a tilde denotes a frequency-domain quantity and $\Omega = \omega - \omega_0 - k_0 u r^2/2f_0^2$. The wave front curvature applied by the nominal focusing lens appears as the radially varying phase in the exponent. The time-dependent focusing appears as a radially dependent frequency shift, or spatial chirp, i.e., the argument of $\tilde{\Theta}$. Thus, this type of flying focus pulse can be created by applying a frequency shift, i.e., $\omega \rightarrow \omega - \omega_0 u r^2/2cf_0^2$, at each radius. This shift supplies the bandwidth needed to support the effective duration of the intensity peak, i.e., $\tau = k_0 w_0^2/c|u|$, in the far field. In all cases of interest, $|u|w_l^2/2f_0^2 \ll 1$, such that the frequency shift contributes only a small broadening to the emitted harmonics in NLTS.

As an example, consider drift-free nonlinear Thomson scattering using a $\lambda_0 = 1.054\,\mu$m wavelength pulse with $U_p = 580$ J of energy and a 2.5 MeV ($\gamma_0 = 5$) electron. Once the peak intensity and $\alpha$ are specified, all other parameters are determined. Consistent with the parameters used in the main text, a peak intensity of $I = 1.1 \times 10^{19}$ W/cm$^2$ ($a_0 = 3$) and $\alpha = 1.2$ will be used. This value of $\alpha$ ensures that the transverse ponderomotive force gently focuses electrons.

For the intensity peak to overtake the electron, it must travel a distance $L = \gamma_0^2 c\tau = 2\gamma_0^2 k_0 w_0^2$, where $|u| \approx \frac{1}{2}$ has been used ($v_I \approx c$ and $v_g = -c$). Using this expression for $L$ in the pulse energy,

$$U_p = \pi(1 + \alpha^2) w_0^2 L I/c, \tag{B5}$$

determines the focal spot size $w_0 = 5\,\mu$m, which, in turn, determines the focal range $L = 7.5$ mm and $f$ number $F_N = 7$. From the focal range, one can find the pulse duration $T = \kappa L/|u| = 60$ ps, where $\kappa = 1.2$ is a numerical factor associated with the functional form chosen for $\Theta(\eta)$. In terms of Eqs. (B3) and (B4), this design requires a maximum frequency shift of $\omega_0 u r^2/2cf_0^2 \sim 4 \times 10^{12}$ rad/s.

Figure 5 shows the results of propagation simulations that demonstrate the flying focus for these parameters using Eqs. (B3) and (B4) as initial conditions. As designed, the intensity peak moves through the pulse at a velocity $v_I = c^2/v_0$ over a distance of ~8 mm and with an effective duration of $\tau = 1$ ps. The orthogonally polarized Laguerre Gaussian modes form a bowl-shaped intensity profile with a width of ≈4 $\mu$m. The nearly propagation invariant Lorentzian temporal profile with respect to the coordinate $\xi = z - v_I t$, effective duration, and transverse shape are all consistent with the analytical model presented in the Appendix A.

Reference [48] describes an optical system for spatiotemporal pulse shaping that can create a time-dependent focal length and the electric field profiles displayed in Eqs. (B3) and (B4). The "flying focus X" uses a "stencil" pulse to spatiotemporally structure the flying focus pulse through cross-phase modulation in a shaped Kerr lens. This particular optical system is limited to peak focal intensities of $\sim 10^{17}$ W/cm$^2$. Designing an optical system that can produce the same properties at higher intensity is an active field of research.

The simulations solve for the evolution of the pulse in two steps. The first step uses a frequency domain Fresnel integral, as described in the Appendix of Ref. [61], to propagate the envelope of the pulse from the near field to the far

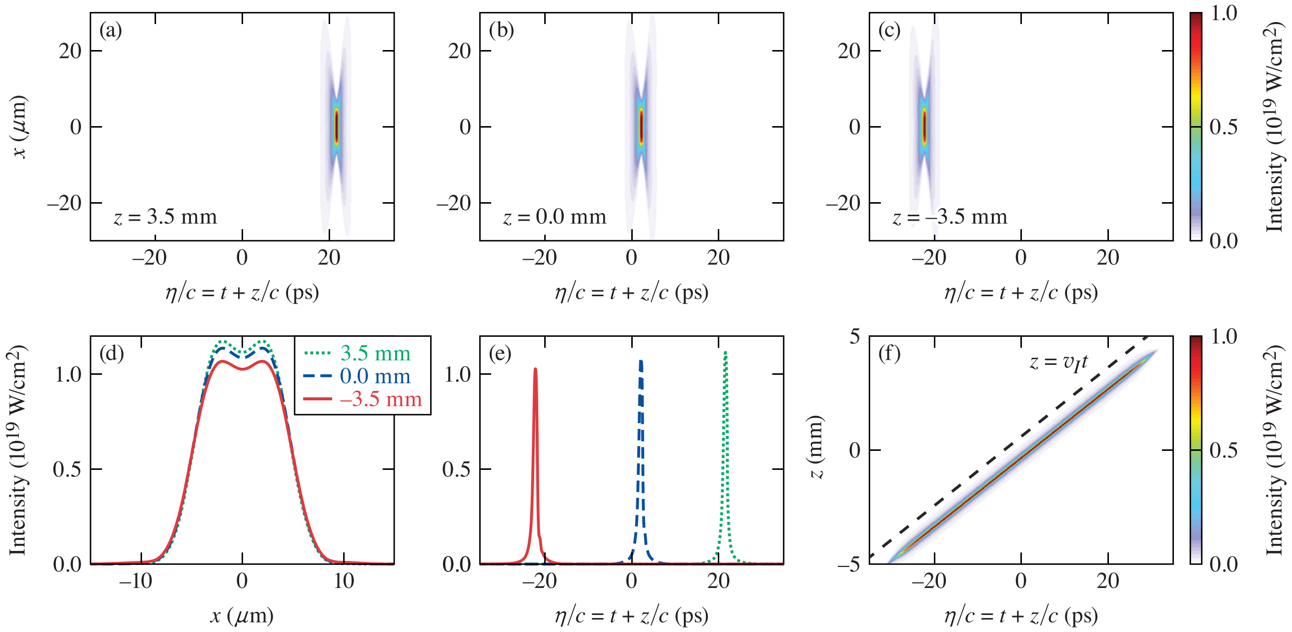

FIG. 5. Example of a practical flying focus design for drift-free NLTS. (a)–(c) Evolution of the propagation invariant intensity profile across the interaction region $L$. The flying focus pulse travels from right to left, while its intensity peak travels from left to right. The intensity peak counterpropagates with respect to the phase fronts and maintains a stationary profile in the frame $\xi = z - v_I t$. (d) The bowl-shaped transverse intensity profile formed by the orthogonally polarized Laguerre-Gaussian modes. (e) The on-axis ($r = 0$) temporal profile of the intensity peak. (f) On-axis intensity as a function of $z$ and $\eta$. The dashed line illustrates the slope of the expected trajectory. Note that the abscissa is $\eta/c = t + z/c$ and that a laboratory frame trajectory $z = v_I t$ is equivalent to $z = v_g v_I \eta / c(v_g - v_I)$.

field:

$$\tilde{\boldsymbol{E}}(\mathbf{x}_\perp, z, \omega) = \frac{k_\omega}{2\pi i(f_0 - z)} \int \exp\left[\frac{ik_\omega}{2(f_0 - z)}(\mathbf{x}_\perp - \mathbf{x}'_\perp)^2\right] \times \tilde{\boldsymbol{E}}(\mathbf{x}'_\perp, f_0, \omega)\, d\mathbf{x}'_\perp, \tag{B6}$$

where $k_\omega = \omega/c$. This allows for separate spatial resolution in the near and far fields, which greatly reduces the number of grid points compared to numerically solving the wave equation over the entire propagation distance [61]. The second step uses the modified paraxial wave equation to propagate the pulse through the far field,

$$[2(ik_0 - \partial_\eta)\partial_z - \nabla_\perp^2]\boldsymbol{E}(\mathbf{x}_\perp, z, \eta) = 0. \tag{B7}$$

The results shown in Fig. 5 were obtained from this second step. The mixed space-time derivative in Eq. (B7) ensures that effects such as radial group delay and angular dispersion are modeled correctly. The simulations used a nominal focal length of $f_0 = 0.51$ m and an initial spot size $w_l = 3.6$ mm.

## APPENDIX C: RADIATION PROPERTIES

The radiation emitted in NLTS results from the acceleration of an electron in the fields of an intense laser pulse. These fields were modeled using a vector potential $\mathbf{A}$ that captures the salient features of a spatiotemporally shaped pulse: $\mathbf{a} = a(z - \beta_I t)\cos(z + t)\hat{\mathbf{x}}$, where $\mathbf{a} = e\mathbf{A}/m_e c$, $a(z - \beta_I t)$ represents an envelope traveling at the ponderomotive velocity $\beta_I$, and time and space have been normalized to $\omega_0$ and $\omega_0/c$, respectively. In response to the fields of the laser pulse, the electron momentum $\mathbf{u}$ and energy $\gamma$ evolve according to the equations of motion:

$$\frac{d\mathbf{u}}{dt} = \frac{\partial \mathbf{a}}{\partial t} - \frac{\mathbf{u}}{\gamma} \times (\nabla \times \mathbf{a}), \tag{C1}$$

$$\frac{d\gamma}{dt} = -\frac{\mathbf{u}}{\gamma} \cdot \frac{\partial \mathbf{a}}{\partial t}, \tag{C2}$$

where momentum and energy have been normalized to $m_e c$ and $m_e c^2$, respectively. For an electron initially outside of the pulse envelope with no transverse momentum, the transverse component of Eq. (C1) provides $u_x = \mathrm{a}$, where $\mathrm{a} = \hat{\mathbf{x}} \cdot \mathbf{a}$.

The coordinate transformations $\eta = z + t$ and $\xi = z - \beta_I t$ facilitate analysis of the longitudinal momentum and energy. In terms of these coordinates, $\mathbf{a} = a(\xi)\cos(\eta)\hat{\mathbf{x}}$, and

$$\left[\frac{\partial}{\partial \eta} + \left(\frac{\beta_z - \beta_I}{1 + \beta_z}\right)\frac{\partial}{\partial \xi}\right]u_z = -\frac{1}{2(1 + \beta_z)\gamma}\left(\frac{\partial}{\partial \eta} + \frac{\partial}{\partial \xi}\right)\mathrm{a}^2, \tag{C3}$$

$$\left[\frac{\partial}{\partial \eta} + \left(\frac{\beta_z - \beta_I}{1 + \beta_z}\right)\frac{\partial}{\partial \xi}\right]\gamma = -\frac{1}{2(1 + \beta_z)\gamma}\left(\frac{\partial}{\partial \eta} - \beta_I\frac{\partial}{\partial \xi}\right)\mathrm{a}^2, \tag{C4}$$

where $\beta_z = u_z/\gamma$. For a typical spatiotemporally shaped pulse, the duration of the intensity peak is much longer than the optical period, i.e., $|\partial_\eta \mathbf{a}| \gg |\partial_\xi \mathbf{a}|$. Further, the electron travels at a relativistic velocity ($\beta_z \lesssim 1$) that is antiparallel to the phase velocity of the pulse. Together, these allow for an approximate solution to Eqs. (C4) and (C2) based on a multiple-timescale approach, i.e., using $|\partial_\eta| \gg |\partial_\xi|$.

To lowest order, one finds the local conservation equation $\partial_\eta(\gamma + u_z) = 0$. Integrating this equation provides the local Hamiltonian $h$ of the electron in a frame moving with the phase velocity, $\gamma + u_z = h(\xi)$, or, equivalently, $\langle\gamma\rangle + \langle u_z\rangle = h(\xi)$, where $\langle\cdot\rangle$ denotes an average over the rapidly varying phase of the laser pulse. To next order, one finds the slowly varying conservation equation $\partial_\xi(\gamma - \beta_I u_z) = 0$, which, upon phase averaging, becomes $\partial_\xi(\langle\gamma\rangle - \beta_I\langle u_z\rangle) = 0$ [49,62]. For an electron with an initial momentum $\mathbf{u}_0 = |\beta_0|\gamma_0\hat{\mathbf{z}}$, $\langle\gamma\rangle - \beta_I\langle u_z\rangle = \gamma_0(1 - \beta_I\beta_0)$. Using this to eliminate $\langle u_z\rangle$ in $h$ yields Eq. (1).

With an expression for $h$, one can follow the derivation presented by Esarey *et al.* [19] for the electron trajectory and radiation properties; however, unlike in the work by Esarey *et al.*, these properties are dynamic, varying with $\xi$ through the dependence of $h$ on $a(\xi)$. For brevity of notation, reference to the explicit $\xi$ dependence of slowly varying quantities will now be dropped. From $\gamma + u_z = h$ and $u_x = \mathrm{a}$, one can find the transverse and longitudinal velocities: $\beta_x = \mathrm{a}/\gamma$ and $\beta_z = (h^2 - 1 - \mathrm{a}^2)/(h^2 + 1 + \mathrm{a}^2)$. The electron coordinates then evolve according to $\dot{x} = \mathrm{a}/h$ and $\dot{z} = \frac{1}{2}(1 - h^{-2} - \mathrm{a}^2)$, where an overdot represents differentiation with respect to $\eta$ and $d\eta = (1 + \beta_z)dt$ has been used. Upon integrating,

$$x(\eta) = x_0 \sin(\eta), \tag{C5}$$

$$z(\eta) = \frac{1}{2}\left(1 - \frac{\langle\gamma_\perp^2\rangle}{h^2}\right)\eta - z_0 \sin(2\eta) \tag{C6}$$

to lowest order in the timescale expansion, where $x_0 = a/h$, $z_0 = a^2/8h^2$, and $\langle\gamma_\perp^2\rangle = 1 + \frac{1}{2}a^2$. The oscillating terms trace out a figure eight—a general feature of electron motion in NLTS. The amplitude of these oscillations $(x_0, z_0)$ depends on the local values of $a$ and $h$. Substituting $\eta = z + t$ into Eq. (C6), rearranging terms, and differentiating with respect to $t$ provide the longitudinal drift velocity, $\beta_d = (h^2 - \langle\gamma_\perp^2\rangle)/(h^2 + \langle\gamma_\perp^2\rangle)$.

The local values of $a$ and $h$ determine all properties of the emitted radiation. Acting like a nonlinear, relativistic moving mirror, the electron emits harmonics of the twice-Doppler upshifted frequency of the laser pulse:

$$\omega_n = n\frac{1 + \beta_d}{1 - \beta_d} = n\frac{h^2}{\langle\gamma_\perp^2\rangle}. \tag{C7}$$

The harmonics range over a bandwidth characterized by the invariant critical integer $n_c = \frac{3}{4}a^3$, such that $\omega_b = \frac{3}{4}a^3\omega_1$. The radiation is spread over an angle $\theta_e$ determined by the bounds of the oscillations: $\theta_e \sim |z_0/x_0| = \frac{1}{8}ah^{-1}$. Finally, the phase-averaged radiated power $\langle P\rangle$ is calculated using the relativistic Larmor formula, which yields $\langle P\rangle = \frac{r_e}{3}h^2a^2$, where $r_e$ is the classical electron radius. For an alternative derivation of the radiation properties, one can compute the curvature of the electron trajectory from Eqs. (C5) and (C6) and use the general expressions found in Ref. [63].

For Figs. 2 and 3, the radiation properties were calculated using the peak vector potential $a_0$. To calculate the angular distribution of the radiated power (Fig. 3), Eq. (36) in Ref. [19] was integrated over frequency. The resulting expression, a summation over an infinite number of harmonics, is proportional to the duration of the interaction. This duration was divided out, providing an expression for the power instead of the energy. The summation was performed numerically by truncating at $n_{\max} = 4n_c = 3a_0^3$. Additional summations performed with larger values of $n_{\max}$ confirmed that harmonics beyond $4n_c$ have a negligible effect on the result. When integrated over the solid angle $\Omega$, the resulting power was in excellent agreement with independent calculations that used the relativistic Larmor formula. Further, the angular distribution was compared to calculations that used electron trajectories directly in the Liénard-Wiechert potential. The electron motion was evolved in the model vector potential using the algorithm detailed in Ref. [64], while the Liénard-Wiechert potential was calculated using the algorithm described in Ref. [65]. At different angles, the resulting spectrum was integrated over frequency and divided by the duration of the interaction confirming the distributions displayed in Fig. 3.

## APPENDIX D: OSIRIS SIMULATIONS

The two-dimensional OSIRIS [58] simulations were performed in a moving frame using a nonevolving laser pulse. Specifically, the transverse vector potential was given by $\mathbf{a} = a(z - \beta_I t)\cos(z + t)\hat{\mathbf{x}}$. The shape function $a$ had a constant flat-top region where $a = a_0$ surrounded by symmetric rising and falling edges defined by a smooth fifth order ramping polynomial. For simulations of NPC, the rise and fall times of the pulse were 5, and the total length was 40 (length and time are in units of $c\omega_0^{-1}$ or $\omega_0^{-1}$). For conventional NLTS, a longer pulse was used to ensure a comparable interaction length; the rise and fall times were 100 with a total length of 2340. The simulation box size was 120 × 60 in the longitudinal ($z$) and transverse ($x$) directions, respectively, with cell sizes of $\Delta z = 0.125$ and $\Delta x = 0.25$. A small time step, $\Delta t = 0.0055$, was required to resolve the electron motion and ensure sufficient data to populate the RADIO diagnostic [38]. The total number of spatial cells was 230 400 with one particle per cell. For the radiation diagnostic RADIO, the temporal step size was $\Delta t_R = 0.00153$, while the angular step was 0.00078 rad.

[1] R. W. Schoenlein, S. Chattopadhyay, H. H. W. Chong, T. E. Glover, P. A. Heimann, C. V. Shank, A. A. Zholents, and M. S. Zolotorev, Science **287**, 2237 (2000).

[2] F. Pfeiffer, T. Weitkamp, O. Bunk, and C. David, Nat. Phys. **2**, 258 (2006).

[3] K. J. Gaffney and H. N. Chapman, Science **316**, 1444 (2007).

[4] T. R. M. Barends *et al.*, Science **350**, 445 (2015).

[5] A. Barty, S. Boutet, M. J. Bogan, S. Hau-Riege, S. Marchesini, K. Sokolowski-Tinten, N. Stojanovic, R. Tobey, H. Ehrke, A. Cavalleri, S. Düsterer, M. Frank, S. Bajt, B. W. Woods, M. M. Seibert, J. Hajdu, R. Treusch, and H. N. Chapman, Nat. Photonics **2**, 415 (2008).

[6] J. N. Clark, L. Beitra, G. Xiong, A. Higginbotham, D. M. Fritz, H. T. Lemke, D. Zhu, M. Chollet, G. J. Williams,

M. Messerschmidt, B. Abbey, R. J. Harder, A. M. Korsunsky, J. S. Wark, and I. K. Robinson, Science **341**, 56 (2013).
[7] A. Ringwald, Phys. Lett. B **510**, 107 (2001).
[8] R. Alkofer, M. B. Hecht, C. D. Roberts, S. M. Schmidt, and D. V. Vinnik, Phys. Rev. Lett. **87**, 193902 (2001).
[9] J. B. Hastings, D. P. Siddons, U. van Bürck, R. Hollatz, and U. Bergmann, Phys. Rev. Lett. **66**, 770 (1991).
[10] M. Seto, Y. Yoda, S. Kikuta, X. W. Zhang, and M. Ando, Phys. Rev. Lett. **74**, 3828 (1995).
[11] P. Suortti and W. Thomlinson, Phys. Med. Biol. **48**, R1 (2003).
[12] M.-C. Biston, A. Joubert, J.-F. Adam, H. Elleaume, S. Bohic, A.-M. Charvet, F. Estève, N. Foray, and J. Balosso, Cancer Res. **64**, 2317 (2004).
[13] P. Montay-Gruel, A. Bouchet, M. Jaccard, D. Patin, R. Serduc, W. Aim, K. Petersson, B. Petit, C. Bailat, J. Bourhis, E. Bräuer-Krisch, and M.-C. Vozenin, Radiother. Oncol. **129**, 582 (2018).
[14] P. Emma *et al.*, Nat. Photonics **4**, 641 (2010).
[15] F. Tavella, N. Stojanovic, G. Geloni, and M. Gensch, Nat. Photonics **5**, 162 (2011).
[16] D. Castelvecchi, Nature (London) **525**, 15 (2015).
[17] E. S. Sarachik and G. T. Schappert, Phys. Rev. D **1**, 2738 (1970).
[18] P. Sprangle, A. Ting, E. Esarey, and A. Fisher, J. Appl. Phys. **72**, 5032 (1992).
[19] E. Esarey, S. K. Ride, and P. Sprangle, Phys. Rev. E **48**, 3003 (1993).
[20] S.-Y. Chen, A. Maksimchuk, and D. Umstadter, Nature (London) **396**, 653 (1998).
[21] A. Rousse, K. T. Phuoc, R. Shah, A. Pukhov, E. Lefebvre, V. Malka, S. Kiselev, F. Burgy, J.-P. Rousseau, D. Umstadter, and D. Hulin, Phys. Rev. Lett. **93**, 135005 (2004).
[22] J. Seres, E. Seres, A. J. Verhoef, G. Tempea, C. Streli, P. Wobrauschek, V. Yakovlev, A. Scrinzi, C. Spielmann, and F. Krausz, Nature (London) **433**, 596 (2005).
[23] P. Sprangle, B. Hafizi, and J. R. Peñano, Phys. Rev. Spec. Top. Accel. Beams **12**, 050702 (2009).
[24] M. Fuchs, R. Weingartner, A. Popp, Z. Major, S. Becker, J. Osterhoff, I. Cortrie, B. Zeitler, R. Hörlein, G. D. Tsakiris, U. Schramm, T. P. Rowlands-Rees, S. M. Hooker, D. Habs, F. Krausz, S. Karsch, and F. Grüner, Nat. Phys. **5**, 826 (2009).
[25] A. D. Debus, M. Bussmann, M. Siebold, A. Jochmann, U. Schramm, T. E. Cowan, and R. Sauerbrey, Appl. Phys. B **100**, 61 (2010).
[26] S. Cipiccia *et al.*, Nat. Phys. **7**, 867 (2011).
[27] K. Ta Phuoc, S. Corde, C. Thaury, V. Malka, A. Tafzi, J. P. Goddet, R. C. Shah, S. Sebban, and A. Rousse, Nat. Photonics **6**, 308 (2012).
[28] S. Corde, K. Ta Phuoc, G. Lambert, R. Fitour, V. Malka, A. Rousse, A. Beck, and E. Lefebvre, Rev. Mod. Phys. **85**, 1 (2013).
[29] F. Albert, A. G. R. Thomas, S. P. D. Mangles, S. Banerjee, S. Corde, A. Flacco, M. Litos, D. Neely, J. Vieira, Z. Najmudin, R. Bingham, C. Joshi, and T. Katsouleas, Plasma Phys. Controlled Fusion **56**, 084015 (2014).
[30] N. D. Powers, I. Ghebregziabher, G. Golovin, C. Liu, S. Chen, S. Banerjee, J. Zhang, and D. P. Umstadter, Nat. Photonics **8**, 28 (2014).
[31] I. A. Andriyash, R. Lehe, A. Lifschitz, C. Thaury, J.-M. Rax, K. Krushelnick, and V. Malka, Nat. Commun. **5**, 4736 (2014).
[32] S. G. Rykovanov, C. B. Schroeder, E. Esarey, C. G. R. Geddes, and W. P. Leemans, Phys. Rev. Lett. **114**, 145003 (2015).
[33] G. Sarri, D. J. Corvan, W. Schumaker, J. M. Cole, A. Di Piazza, H. Ahmed, C. Harvey, C. H. Keitel, K. Krushelnick, S. P. D. Mangles, Z. Najmudin, D. Symes, A. G. R. Thomas, M. Yeung, Z. Zhao, and M. Zepf, Phys. Rev. Lett. **113**, 224801 (2014).
[34] J. P. Palastro, D. Kaganovich, and D. Gordon, Phys. Plasmas **22**, 063111 (2015).
[35] D. J. Stark, T. Toncian, and A. V. Arefiev, Phys. Rev. Lett. **116**, 185003 (2016).
[36] W. Yan, C. Fruhling, G. Golovin, D. Haden, J. Luo, P. Zhang, B. Zhao, J. Zhang, C. Liu, M. Chen, S. Chen, S. Banerjee, and D. Umstadter, Nat. Photonics **11**, 514 (2017).
[37] K. Dupraz *et al.*, Phys. Open **5**, 100051 (2020).
[38] J. Vieira, M. Pardal, J. T. Mendonça, and R. A. Fonseca, Nat. Phys. **17**, 99 (2021).
[39] K. Deitrick, G. H. Hoffstaetter, C. Franck, B. D. Muratori, P. H. Williams, G. A. Krafft, B. Terzić, J. Crone, and H. Owen, Phys. Rev. Accel. Beams **24**, 050701 (2021).
[40] G. A. Krafft, Phys. Rev. Lett. **92**, 204802 (2004).
[41] H. E. Kondakci and A. F. Abouraddy, Nat. Photonics **11**, 733 (2017).
[42] A. Sainte-Marie, O. Gobert, and F. Quere, Optica **4**, 1298 (2017).
[43] D. H. Froula, D. Turnbull, A. S. Davies, T. J. Kessler, D. Haberberger, J. P. Palastro, S.-W. Bahk, I. A. Begishev, R. Boni, S. Bucht, J. Katz, and J. L. Shaw, Nat. Photonics **12**, 262 (2018).
[44] A. Debus, R. Pausch, A. Huebl, K. Steiniger, R. Widera, T. E. Cowan, U. Schramm, and M. Bussmann, Phys. Rev. X **9**, 031044 (2019).
[45] J. P. Palastro, J. L. Shaw, P. Franke, D. Ramsey, T. T. Simpson, and D. H. Froula, Phys. Rev. Lett. **124**, 134802 (2020).
[46] C. Caizergues, S. Smartsev, V. Malka, and C. Thaury, Nat. Photonics **14**, 475 (2020).
[47] T. T. Simpson, D. Ramsey, P. Franke, N. Vafaei-Najafabadi, D. Turnbull, D. H. Froula, and J. P. Palastro, Opt. Express **28**, 38516 (2020).
[48] T. T. Simpson, D. Ramsey, P. Franke, K. Weichman, M. V. Ambat, D. Turnbull, D. H. Froula, and J. P. Palastro, Opt. Express **30**, 9878 (2022).
[49] D. Ramsey, P. Franke, T. T. Simpson, D. H. Froula, and J. P. Palastro, Phys. Rev. E **102**, 043207 (2020).
[50] A. Di Piazza, Phys. Rev. A **103**, 012215 (2021).
[51] I. Ghebregziabher, B. A. Shadwick, and D. Umstadter, Phys. Rev. Spec. Top. Accel. Beams **16**, 030705 (2013).
[52] B. Terzić, K. Deitrick, A. S. Hofler, and G. A. Krafft, Phys. Rev. Lett. **112**, 074801 (2014).
[53] S. G. Rykovanov, C. G. R. Geddes, C. B. Schroeder, E. Esarey, and W. P. Leemans, Phys. Rev. Accel. Beams **19**, 030701 (2016).
[54] D. Seipt, V. Y. Kharin, and S. G. Rykovanov, Phys. Rev. Lett. **122**, 204802 (2019).
[55] A. Di Piazza, C. Müller, K. Z. Hatsagortsyan, and C. H. Keitel, Rev. Mod. Phys. **84**, 1177 (2012).
[56] J. Mendonça, L. Silva, and R. Bingham, J. Plasma Phys. **73**, 627 (2007).
[57] D. H. Froula, J. P. Palastro, D. Turnbull, A. Davies, L. Nguyen, A. Howard, D. Ramsey, P. Franke, S.-W. Bahk, I. A. Begishev, R. Boni, J. Bromage, S. Bucht, R. K. Follett, D. Haberberger, G. W. Jenkins, J. Katz, T. J. Kessler, J. L. Shaw, and J. Vieira, Phys. Plasmas **26**, 032109 (2019).

[58] R. A. Fonseca, L. O. Silva, F. S. Tsung, V. K. Decyk, W. Lu, C. Ren, W. B. Mori, S. Deng, S. Lee, T. Katsouleas, and J. C. Adam, in *Computational Science—ICCS 2002*, edited by P. M. A. Sloot, A. G. Hoekstra, C. J. K. Tan, and J. J. Dongarra (Springer, Berlin, 2002), pp. 342–351.

[59] J. L. Chaloupka and D. D. Meyerhofer, Phys. Rev. Lett. **83**, 4538 (1999).

[60] G. V. Stupakov and M. S. Zolotorev, Phys. Rev. Lett. **86**, 5274 (2001).

[61] J. P. Palastro, D. Turnbull, S.-W. Bahk, R. K. Follett, J. L. Shaw, D. Haberberger, J. Bromage, and D. H. Froula, Phys. Rev. A **97**, 033835 (2018).

[62] C. J. McKinstrie and E. A. Startsev, Phys. Rev. E **54**, R1070 (1996).

[63] J. D. Jackson, *Classical Electrodynamics*, 3rd ed. (Wiley, New York, 1998).

[64] D. Gordon and B. Hafizi, Comput. Phys. Commun. **258**, 107628 (2021).

[65] A. Thomas, Phys. Rev. Spec. Top. Accel. Beams **13**, 020702 (2010).

*Correction:* Equations (A2), (A3), and (A4) contained minor errors and have been fixed.

*Second Correction:* Equation (1) contained a minor error and has been fixed.